The Astrophysical Journal, 602:436–445, 2004 February 10

ULTRAVIOLET OSCILLATIONS IN THE CHROMOSPHERE OF THE QUIET SUN

R. T. James McAteer,[1] Peter T. Gallagher,[1,2] D. Shaun Bloomfield,[1] David R. Williams,[1,3]
Mihalis Mathioudakis,[1] and Francis P. Keenan[1]
Received 2003 July 25; accepted 2003 October 19

ABSTRACT

Quiet-Sun oscillations in the four *Transition Region and Coronal Explorer* (*TRACE*) ultraviolet passbands centered on 1700, 1600, 1216, and 1550 Å are studied using a wavelet-based technique. Both network and internetwork regions show oscillations with a variety of periods and lifetimes in all passbands. The most frequent network oscillation has a period of 283 s, with a lifetime of 2–3 cycles in all passbands. These oscillations are discussed in terms of upwardly propagating magnetohydrodynamic wave models. The most frequent internetwork oscillation has a period of 252 s, again with a lifetime of 2–3 cycles, in all passbands. The tendency for these oscillations to recur in the same position is discussed in terms of "persistent flashers." The network contains greater oscillatory power than the internetwork at periods longer than 300 s in the low chromosphere. This value is shown to decrease to 250 s in the high chromosphere. The internetwork also displays a larger number of short-lifetime, long-period oscillations than the network, especially in the low chromosphere. Both network and internetwork regions contain a small number of nonrecurring long-lifetime oscillations.

Subject headings: methods: statistical — Sun: chromosphere — Sun: oscillations — Sun: photosphere — Sun: UV radiation

1. INTRODUCTION

The subject of chromospheric heating is one of the most studied and yet poorly understood areas of solar physics. A temperature minimum at $\sim$500 km above the photosphere, and the subsequent reversal of the temperature profile, suggests that some unknown heating mechanism must be present to balance the energy lost by radiation. As this mechanism cannot be due to either conduction or radiation (Narain & Agarwal 1994), chromospheric heating theories have mainly concentrated on heating via the dissipation of energy carried by waves. The mode of these waves, whether standing or traveling, the dominant restoring force (magnetic, gas pressure, gravity, etc.), and the resulting oscillations of the chromospheric plasma have been the subject of much deliberation (see reviews by Rutten & Uitenbroek 1991; Rutten 1999).

In the chromosphere, the quiet Sun displays a distinct network appearance identical to the supergranular cell structure in Dopplergrams (Leighton, Noyes, & Simon 1962). The nature of supergranular flow results in magnetic flux coalescing at cell vertices, with replenishment of flux occurring on the scale of a few days to a week (Schrijver et al. 1998). This creates a dense collection of flux tubes (Berger et al. 1998; Lites, Rutten, & Berger 1999) at these vertices and is observable as kilogauss fields in magnetograms. In time-integrated images of the chromosphere, the network is only partially defined as patches of increased intensity (network bright points), which display a one-to-one spatial correlation with this underlying photospheric magnetic field (Cauzzi, Falchi, & Falciani 2000; McAteer et al. 2003). On the other hand, the internetwork is mainly field-free and appears dark on time-integrated images of the chromosphere.

This spatial dichotomy between the network and internetwork is also apparent in the Fourier spectrum of light curves from these two regions, leading to the suggestion that different heating mechanisms may dominate in each region (Gallagher et al. 1999). The internetwork contains oscillations with periodicities around 180 s (a broad 3–8 mHz peak in the Fourier spectrum: the acoustic band), intermittently present in small grains, and with a good correlation between the photosphere and the chromosphere (Lites, Rutten, & Kalkofen 1993). Some work shows the existence of nodal planes and hence standing waves (e.g., Kneer & von Uexküll 1993; Deubner, Waldschik, & Steffens 1996). Other studies show a directly proportional increase of phase lag with frequency between lines formed at different heights in the atmosphere (e.g., Judge, Tarbell, & Wilhelm 2001; Wikstøl et al. 2000). This suggests the presence of upwardly propagating acoustic waves, which have been successfully modeled by Carlsson & Stein (1992, 1997). Brandt et al. (1992) suggest a scenario in which there are two types of grains: one with a long-term memory, termed "persistent flashers," with a magnetic dependence; and a second, 5–10 times more common, with no spatial memory or magnetic dependence. This may explain the difference between the conclusions reached by Worden, Harvey, & Shine (1999) and Lites et al. (1999), who suggest no correlation between the small internetwork magnetic fields and the chromospheric grains, and those of Sivaraman et al. (2000), who found a strong correlation between the internetwork grains and magnetic fields.

Longer period network oscillations (5–20 minutes) have not benefited from similarly detailed simulations, mainly because of the difficulty of modeling the chromospheric plasma in the presence of the kilogauss magnetic fields (Bogdan et al. 2003). Current theories of network heating suggest that the magnetic field is critical, and these fall into three main categories: (1) in situ resistive dissipation from the stochastic rearrangement of magnetic field lines (Kneer & von Uexküll 1985, 1986); (2) upwardly propagating transverse MHD waves coupling, and hence transferring power, to

[1] Department of Pure and Applied Physics, Queen's University Belfast, Belfast BT7 1NN, Northern Ireland, UK; j.mcateer@qub.ac.uk.
[2] L-3 Communications GSI, NASA Goddard Space Flight Center, Greenbelt, MD 20771.
[3] Mullard Space Science Laboratory, Holmbury St. Mary, Dorking, Surrey RH5 6NT, UK.

longitudinal waves, which can then form shocks (Kalkofen 1997; Hasan & Kalkofen 1999; Hasan et al. 2003); (3) resistive dissipation of Pedersen currents, driven by longitudinal MHD waves (Goodman 2000). Observations show a poor temporal correlation between chromospheric network oscillations and those in the underlying photosphere (Lites et al. 1993). Wavelet-based studies (Bocchialini & Baudin 1995; Baudin, Bocchialini, & Koutchmy 1996; McAteer et al. 2003; Bloomfield et al. 2003) show the existence of mainly upwardly propagating (but also some downwardly propagating) waves in the chromosphere at speeds close to the sound speed. Furthermore, the tendency of oscillations to occur in the very center of network elements (McAteer et al. 2002), combined with a lack of both intensity and oscillatory power near, but not directly above, photospheric network elements (termed "magnetic shadows"), suggests the existence of mode conversion of acoustic waves as they interact with the magnetic canopy (Judge et al. 2001; McIntosh & Judge 2001; McIntosh, Fleck, & Judge 2003).

We present an automated wavelet analysis approach (originally applied to Coronal Diagnostic Spectrometer [CDS; Harrison et al. 1995] data by Ireland et al. 1999) to *Transition Region and Coronal Explorer* (*TRACE*; Handy et al. 1999b) quiet-Sun UV oscillations for both the network and internetwork and discuss the results in each region in relation to the above heating mechanisms. When studying quiet-Sun data, wavelet analysis has two specific benefits over the Fourier transform. First, the intermittency of the oscillations present (Banerjee et al. 2001; Hansteen, Betta, & Carlsson 2000) means that their Fourier power may be swamped by the much longer nonperiodic component, whereas wavelet analysis provides localized temporal information. Second, quiet-Sun data sets are difficult to align compared to active region data sets because of a relative lack of features. Again, the time-localized nature of wavelet analysis is better suited than Fourier analysis to dealing with frames that may not be perfectly aligned (Ireland et al. 1999). In order to reduce alignment problems, *TRACE* was used to provide long-duration observations of the Sun, free of atmospheric distortions. The large field of view (FOV) of *TRACE* makes it very useful for quiet-Sun studies, where it provides a larger spatial sample than slit-based spectrometers (e.g., SUMER, CDS). The large passbands of *TRACE* also mean that any oscillations present are free from Doppler-shift effects due to plasma motions. Oscillations must therefore be due to changes in temperature and/or density. However, it is noted that the wide passbands make it difficult to estimate their height of formation (HOF), as each passband contains significant contributions from the continuum in addition to line emission. The wide passbands may also lead to phase averaging.

The outline of this paper is as follows. An overview of the data set, including a discussion of the HOF of each passband, is presented in § 2. The alignment procedure, creation of the network/internetwork subsets, and high-pass filtering are discussed in § 3. This is followed by a detailed description of the wavelet analysis routine designed to search for both the periodicity and lifetime of any oscillations in all the pixels in each subset. Section 4 compares the differing results from the network and internetwork, while our conclusions are given in § 5.

2. OBSERVATIONS

A data set from 1999 May 4 containing quiet-Sun images in the four UV passbands (1700, 1600, 1216, and 1550 Å) with a FOV of $128'' \times 320''$ was selected for this study. Further details of the data set can be found in Krijger et al. (2003). A simple investigation into the frame rate stability in each passband resulted in a constant cadence of 40.05 s being assumed for the purpose of both Fourier and wavelet analyses. After image 168 there was a 50 s delay, corresponding to a small change in the FOV as *TRACE* compensated for solar rotation. For this reason, the data were divided into two equal time blocks: block A containing images 1–168, and block B containing images 169–336. This creation of two data blocks was also vital for data analysis (§§ 3.1 and 3.2) and to the search for oscillation recurrence (§§ 4.3). In some cases there were 80 s time gaps between images. It was assumed that this was due to a missing image. These missing images were replaced by an average of the (aligned) preceding and following images. Any images severely contaminated by cosmic rays were cleaned using programs available in the *TRACE* branch of the SolarSoftWare (SSW; Freeland & Handy 1998) tree of IDL.

2.1. *Heights of Formation*

There are well-known difficulties associated with attributing HOFs to emission from broadband filters. Because of the complexity of line emission and continuum, any HOF will vary in both time (e.g., during a flare) and space (e.g., plage/network-internetwork). While realizing the limitations of any assigned HOF, we suggest the following: Previous work with *TRACE* UV data (Judge et al. 2001; Krijger et al. 2001; Handy et al. 1999b) places the 1700 Å band lowest in the atmosphere (UV continuum at $\sim 4-10 \times 10^3$ K, below temperature minimum), followed by the 1600 Å passband (UV continuum at $\sim 4-10 \times 10^3$ K plus Fe II at $\sim 1.3 \times 10^4$ K, temperature minimum). Up to 50% of the signal in the 1216 Å passband is also believed to be UV continuum (Worden et al. 1999), suggesting an HOF around the mid-chromosphere (50% Lyα at $\sim 1-3 \times 10^4$ K, plus 50% UV continuum). The 1550 Å passband has the highest HOF, at $\sim 1 \times 10^5$ K, but with significant contributions from other lines (e.g., Si II at $\sim 1 \times 10^4$ K) and the continuum. These temperatures are approximate, and there is expected to be a degree of overlapping emission between passbands. However, in order to carry out a qualitative discussion of our results, we assume a sequence of increasing HOF of 1700, 1600, 1216, and 1550 Å.

Techniques have been developed to separate both the Lyα (Handy et al. 1999a) and C IV (Handy et al. 1998) emission from the continuum. However, in both cases it is shown that these techniques are only reliable for more intense solar features (e.g., Fig. 6 of Handy et al. 1999a). The bright network will be at the lower limit of this intensity, and the techniques are certainly not applicable to the internetwork without long exposure times. As we wish to compare network and internetwork oscillations, we decided not to apply any continuum removal to the data.

3. DATA ANALYSIS

3.1. *Alignment*

The division of the data into two blocks was vital to compensating for solar differential rotation in the data set (estimated as $1''$ over each 167 image block). Initially, all wavelengths were aligned by calculating the offsets of the middle image of each block to the corresponding 1600 Å image and shifting all images in each wavelength correspondingly. At each

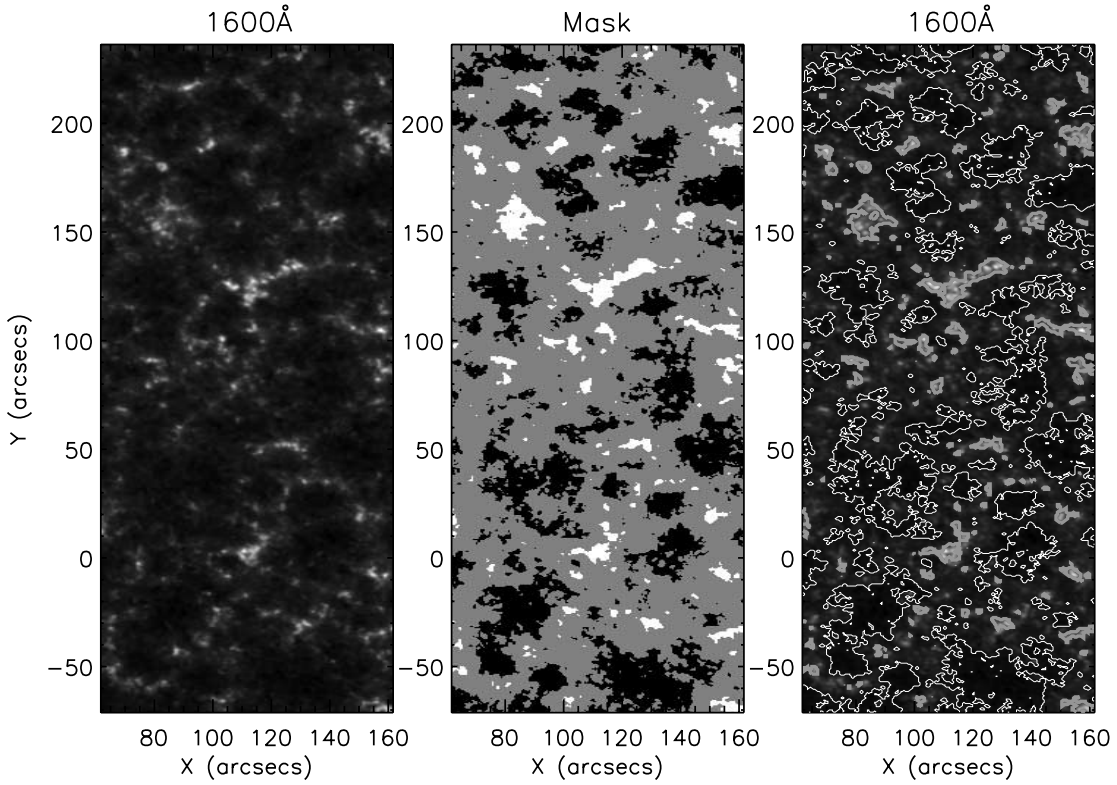

FIG. 1.—*Left*: Time-averaged (data block A) 1600 Å image. *Middle*: Network (*white*) and internetwork (*black*) masks. *Right*: Network (bright) pixels contoured with thick gray lines and internetwork (dark) pixels contoured with thin white lines.

wavelength, all images were then aligned to the middle image of the time series using cross-correlation programs available in SSW. Any large offsets were replaced by the average of the preceding and following offsets, and the cross-correlation was repeated until all offsets were less than 0.2 pixels (i.e., 0.″1). This procedure was carried out for each block separately. Finally, the offset of the middle image of block A to block B was found using the same cross-correlation procedure, and all block B data were shifted by this offset. This resulted in the entire time series, in all four UV wavelengths, being aligned to within 0.″1. Because of solar rotation, several pixel rows and columns were not always present in the data, so that the aligned data FOV was reduced from 256×640 to 215×600 pixel^2.

3.2. *Creation of Network and Internetwork Subsets*

The nature of the network to appear bright in time-averaged images was used to define a network/internetwork mask in a method similar to Krijger et al. (2001). For the aligned 1600 Å data, a time-averaged image was created for each block. For each time-averaged image, a histogram of pixel values was created. Pixels with an intensity below the modal intensity value were defined as internetwork, while those with an intensity value greater than 1 σ above the mean intensity value were defined as network (McAteer et al. 2002; Worden et al. 1999). The subsequent network pixel arrays for block A and block B were compared, and only pixels defined as network in both data blocks were retained. A similar process was carried out for the internetwork. The resulting network and internetwork pixels are displayed in Figure 1. The left image is the time-averaged 1600 Å block A, where the network appears as bright clusters at supergranular cell vertices. The network and internetwork pixels are contoured in the right image, according to the masks in the middle image (where white is the network mask and black is the internetwork mask). These masks were then applied to all four UV passbands.

3.3. *Filtering*

With 167 images at 40.05 s cadence, the Nyquist frequency is 11.1 mHz, and the frequency resolution is 0.13 mHz. After subtracting the mean, this provides a range of detectable periodicity of 90–7692 s. A high-pass filter was employed such that all Fourier power below $\sim$0.6 mHz (above $\sim$1642 s in period space, corresponding to the maximum possible detectable period; see § 3.4, eq. [3], and Fig. 2) was removed. The importance of filtering is to increase the significance of the expected peak around 3–5 minutes by reducing aliasing effects. Filtering was carried out on each light curve by convolution with a suitable Bessel function so as to provide a smooth edge to the filter profile and hence reduce ringing effects.

3.4. *Wavelet Analysis*

A wavelet analysis was carried out on each light curve using a Morlet wavelet of the form

$$\psi(\eta) = \pi^{-1/4} \exp(i\omega_0\eta) \exp\left(\frac{-\eta^2}{2}\right), \quad (1)$$

where $\eta = t/s$ is the dimensionless time parameter, t is the time, s is the scale of the wavelet, $\omega_0 = s\omega$ is the dimensionless frequency parameter ($\omega_0 = 6$, to satisfy the admissibility condition; Farge 1992), and $\pi^{-1/4}$ is a normalization term. For the Morlet wavelet, the Fourier period is $\sim$1.03

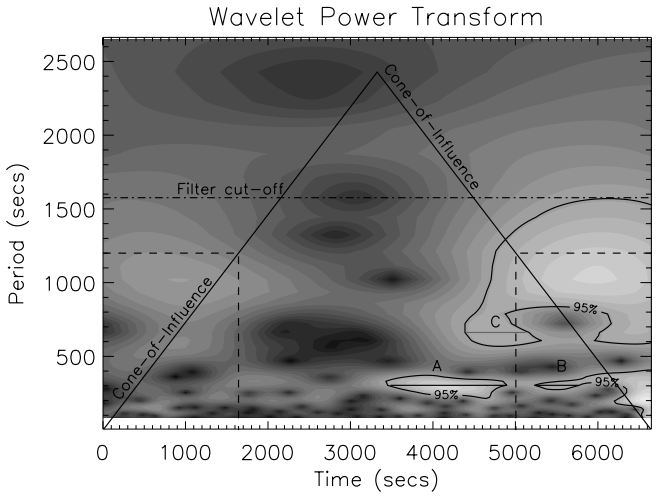

FIG. 2.—Wavelet power transform of a typical network light curve. The two slanted lines define the cone of influence, the size of which at a period of 1200 s is shown by the dashed lines as 1647 s at each end of the time series. The dash-dotted line is at 1624 s, the cutoff of the high-pass filter. The contours are at the 95% confidence level. The three maxima outside the cone of influence are marked A, B, and C, and the solid horizontal lines define their lifetimes.

times the wavelet scale (Torrence & Compo 1998). At each point in time, this provides a real and imaginary part to the wavelet transform. The wavelet power transform is then the square of the absolute value of the wavelet transform. A typical wavelet power transform for a network light curve is shown in Figure 2. Here, the abscissa is time, t, and the ordinate is period, P. This is displayed on a linear intensity scale, such that brighter areas correspond to greater oscillatory power. The contours are at the 95% significance level, and the two slanted lines define the cone of influence (COI). Edge effects are significant above these two lines. The extent of the COI, from the beginning and the end of the time series at each period P, is defined in Torrence & Compo (1998) for the Morlet wavelet as the decorrelation time for a spike in the time series, $t_d = \sqrt{2}P/1.03$ s. For example, for the dashed lines in Figure 2 at $P = 1200$ s, the COI extends from $t = 0$ to 1647 s, and from $t = 5001$ to 6648 s. After creating the wavelet power transform, an automated routine calculated the lifetime and periodicity of any oscillations, following the procedure first described in Ireland et al. (1999). First, all power below the 95% significance level or above the COI lines was removed. The routine then searched for any remaining power maxima. The lifetime of the oscillation at the period of each power maximum is defined as the interval of time from when the power reaches above 95% significance to when it dips below 95% significance again. The lifetime was then divided by the period to give a lifetime in terms of complete cycles. For example, for the oscillatory power in contour A in Figure 2, the lifetime is given by $(4900 - 3500)/300 = 4.67$ cycles. Any oscillations lasting for less than t_d [e.g., for the maxima in contour C in Fig. 2, lifetime $= (5100 - 4400)/650 = 1.08$ cycles] were discarded as possibly being the result of a spike in the time series. From the criterion of a lifetime of at least $\sqrt{2}P/1.03$ outside the COI (of size $2\sqrt{2}P/1.03$), the maximum possible detectable period $P_{\max}$ can be obtained from

$$\frac{3\sqrt{2}P_{\max}}{1.03} = \delta t(N-1), \tag{2}$$

where δt is the cadence and N is the number of data points in the light curve [hence, $\delta t(N-1)$ is the total duration of the light curve]. Rearranging,

$$P_{\max} = \frac{1.03 \times 40.05 \times 167}{3\sqrt{2}} = 1642 \text{ s}. \tag{3}$$

The quantity $P_{\max}$ is shown as the dash-dotted line in Figure 2 and is the value used as the cutoff for the high-pass filter (§ 3.3). The final output from the routine is a list of lifetimes and periodicities for all oscillations in each input light curve.

4. RESULTS AND DISCUSSION

4.1. *Internetwork Oscillations*

A summary of all internetwork oscillations for the first half (block A) of the 1700 Å data is shown in Figure 3. Here the ordinate is the period P as determined from the wavelet analysis. The nature of wavelet analysis means that the values of the period increase logarithmically. The abscissa, l, is the oscillation lifetime binned to integer values. For example, the lifetime of 4.67 cycles discussed above is placed in the 4–5 bin. The horizontal dashed line is at $\sqrt{2}/1.03$ cycles (minimum lifetime), and the vertical dashed line is at the Nyquist frequency, while the two solid vertical lines are at 3 and 5 minutes. The curved dashed line refers to the maximum number of complete cycles that can be observed at each period (due to the finite length of the time series). Figure 3 is plotted on an inverted linear intensity scale, such that darker areas correspond to a larger number of pixels with oscillations at period P, for lifetime l. The four color bands refer to the upper quartile (*black*, >75% of peak value), mid-to-upper quartile (*dark gray*, 50%–75% of peak value), mid-to-lower quartile (*light gray*, 25%–50% of peak value), and lower quartile (*lightest gray*, <25% of peak value). The data have been divided by the number of pixels (hence, the number of light curves) to make all results from the network and internetwork directly comparable.

Figure 3 displays several interesting features. The most common oscillation is a well-defined peak with a period of $\log_{10}(P) = 2.33$ ($P \sim 210$ s), lasting for 2–3 cycles, with an occurrence rate of 0.26 (i.e., 1 in 4 pixels contains an oscillation at this period for this lifetime). There are few oscillations below $\log_{10}(P) = 2.2$ ($P \sim 160$ s), and all the long-lifetime oscillations (LLOs: defined as >8 cycles) occur near the acoustic band [i.e., $\log_{10}(P) \sim 2.2 - 2.5$]. The internetwork results from the other UV passbands display a similar behavior.

By summing Figure 3 over the lifetime axis, we can create occurrence rate curves that are directly comparable to the average Fourier power curves (Fig. 4). These occurrence rate curves have also been divided by a probability correction curve, to account for the fact that short-period oscillations are more likely to be observed (less time to undergo $\sqrt{2}/1.03$ cycles and more light curve outside the COI). In Figure 4 the ordinate is the occurrence per pixel (i.e., average number of cycles) for the top panel and the average Fourier power per pixel for the bottom panel. Both panels share the same abscissa as Figure 3, namely, period on a log scale. Again, the two vertical lines are at 3 and 5 minutes. A simple Gaussian fit (i.e., with no continuum) has been applied to the feature around the acoustic band and overplotted in each case. The Gaussian fit was applied to the region of the curve from where it rises above zero to the minimum around $\log_{10}(P) = 2.6$. The value of the center of the

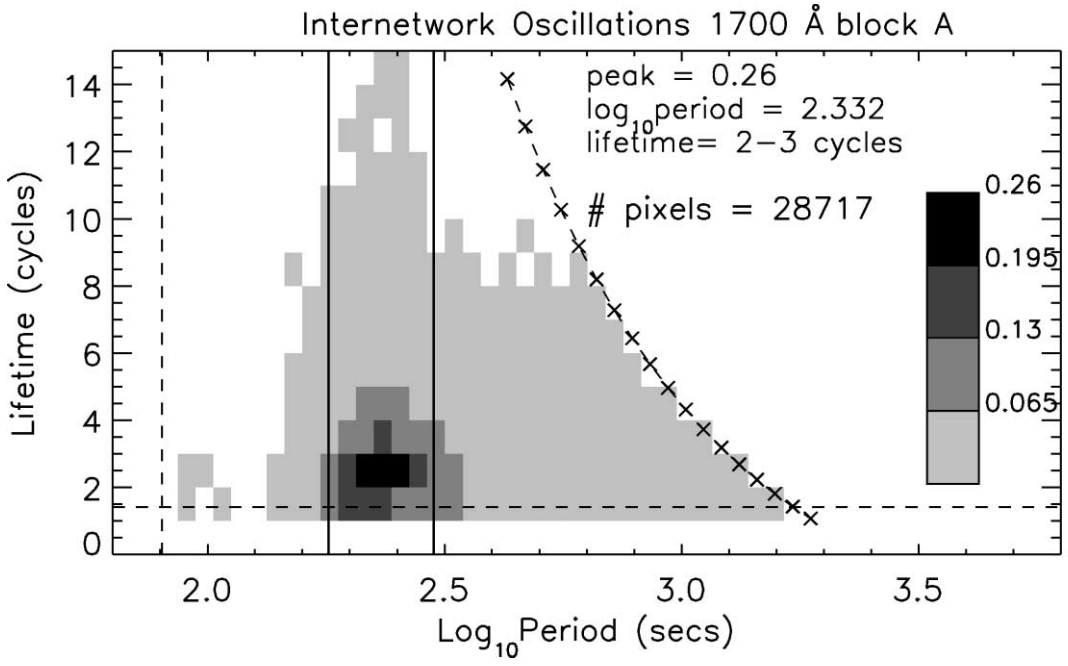

FIG. 3.—Summary of all internetwork oscillations for the 1700 Å block A data set (28,717 pixels). The frequency of occurrence of any oscillation at each period and lifetime is plotted according to the intensity scale on the right. The dashed vertical and horizontal lines are at the Nyquist frequency and minimum lifetime, respectively. The two solid vertical lines are at 3 and 5 minutes. The curved dashed line defines the maximum detectable number of cycles for each period. The four shades of gray correspond to greater than 75%, 50%–75%, 25%–50%, and less than 25% of the maximum value (0.26).

Gaussian fit (COG) and the 1 σ width are displayed in the top right corner of each plot. It should be noted that this width is an indication of the spread of frequencies around the peak. The estimated error in the determination of the position of the COG fit is typically around 0.005 in $\log_{10}(P)$ (i.e., $\delta P \sim 4$ s) and hence much smaller than the 1 σ width.

Figure 4 shows the good agreement between the wavelet analysis and classical Fourier approach. It displays a rise of power (Fourier) and occurrence rate (wavelet) with increasing period, reaching a maximum around $\log_{10}(P) = 2.4$ ($P \sim 250$ s). This value differs from the peak in Figure 3 because of the probability correction curve applied to the data. Both curves reach a minimum around $\log_{10}(P) = 2.6$ ($P \sim 400$ s), followed by a gradual increase at higher periods. Using phase analysis techniques, Krijger et al. (2001) attribute this high period power primarily to internal gravity waves, with some contribution from granular overshoot and the low-frequency tail of acoustic interference. The falloff at $\log_{10}(P) > 3.0$ is due to the high-pass filter applied to the light curves.

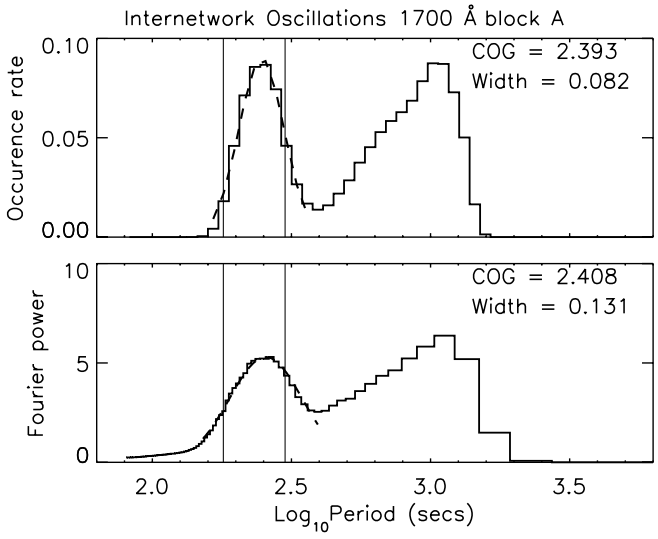

FIG. 4.—Occurrence rate (*top*) and Fourier power (*bottom*) per pixel for all internetwork pixels in the 1700 Å block A data set. In both portions, a Gaussian fit (*dashed line*) is applied to the feature around $\log_{10}(P) = 2.4$, and the center and 1 σ width of this Gaussian fit are displayed at the top right.

4.2. *Network Oscillations*

A summary of all network pixel oscillations from the first half of the 1700 Å data is displayed in Figure 5. In contrast to the results from the internetwork pixels, the most common network oscillation is a well-defined peak with a longer period of $\log_{10}(P) = 2.41$ ($P \sim 260$ s), lasting for 2–3 cycles, with a lower occurrence rate of 0.19 (i.e., 1 in 5 pixels contains an oscillation at this period for this lifetime; the distribution of the occurrence rate is broader in the network). As in the internetwork, there are few oscillations below $\log_{10}(P) = 2.2$ ($P \sim 160$ s), and all the LLOs occur near the acoustic band. However, the network contains an extended tail at the 25%–50% level up to periods of $\log_{10}(P) = 2.9$ ($P \sim 800$ s). Hasan & Kalkofen (1999) suggest a scenario in which kink-mode waves generated in the photospheric network may travel up through the chromosphere before coupling with sausage-mode waves. The extended tail of the network oscillations in Figure 5 may be the oscillatory signature of the kink-mode wave at $P = 534$ s [$\log_{10}(P) = 2.73$]. In the 1216 and 1550 Å passbands, this tail is less evident; hence, these waves may have coupled in the high chromosphere.

Figure 6 repeats the comparison of the wavelet analysis and classical Fourier approaches of Figure 4, but applied to the network data. Figure 6 displays a rise of power (Fourier) and occurrence rate (wavelet) with increasing period, reaching a maximum around $\log_{10}(P) = 2.45$ ($P \sim 280$ s). The two

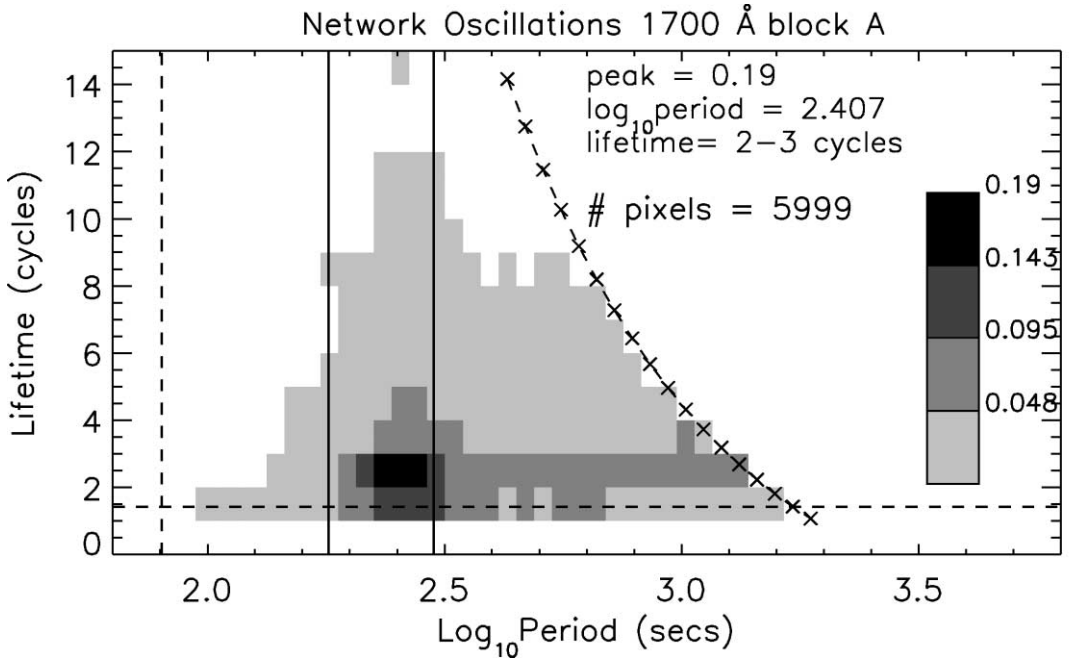

FIG. 5.—Summary of all network oscillations for the 1700 Å block A data set (5999 pixels). The frequency of occurrence of any oscillation at each period and lifetime is plotted according to the intensity scale on the right. The dashed vertical and horizontal lines are at the Nyquist frequency and minimum lifetime, respectively. The two solid vertical lines are at 3 and 5 minutes. The curved dashed line defines the maximum detectable number of cycles for each period. The four shades of gray correspond to greater than 75%, 50%–75%, 25%–50%, and less than 25% of the maximum value (0.19).

curves reach a minimum around $\log_{10}(P) = 2.6$ ($P \sim 400$ s), followed by a gradual increase. Again, the falloff at $\log_{10}(P) > 3.0$ is due to the high-pass filter performed on the light curves.

4.3. *Oscillation Recurrence*

By comparing how many pixels in block A of each wavelength display a similar behavior in block B, it is possible to study whether oscillations of specific period and lifetime occur repeatedly. At each wavelength all network pixels displaying periodicity between 230 and 280 s in block A were selected and compared to network pixels containing periodicity in the same range in block B. This showed a recurrence rate of ~65%–75% in all four UV passbands. This was also carried out for all network pixels displaying oscillations lasting 2–3 cycles at all periods (where the corresponding value was ~75%–85%). A study of all network pixels lasting 2–3 cycles *and* in the range 230–280 s (i.e., at the peak value in the lifetime-period plots) showed ~40% common pixels. As these oscillations are the most frequent, a 40% chance of a recurrence at the same position represents a good candidate for repeated heating of the surrounding plasma.

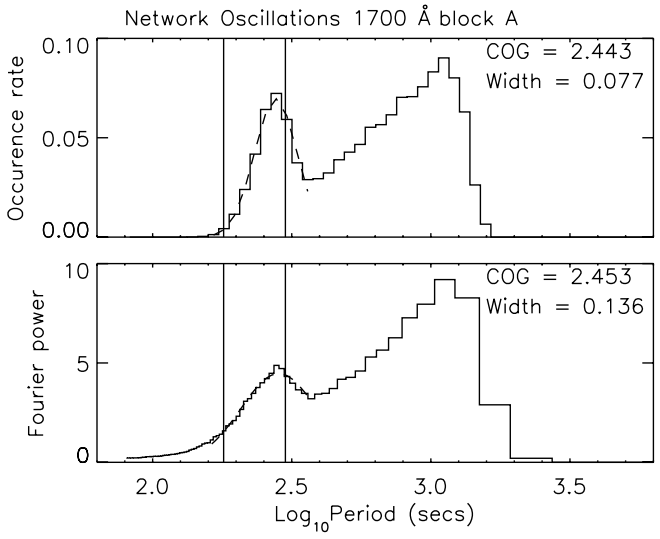

FIG. 6.—Occurrence rate (*top*) and Fourier power (*bottom*) per pixel for all network pixels in the 1700 Å block A data set. In both portions, a Gaussian fit (*dashed line*) is applied to the feature around $\log_{10}(P) = 2.4$, and the center and 1 σ width of this Gaussian fit are displayed at the top right.

In the internetwork, the fraction of pixels showing oscillations recurring in the same location is generally 5%–10% higher than in the network. The internetwork oscillations lasting 2–3 cycles *and* in the range 230–280 s (with a ~50% recurrence rate) may be the persistent flashers first identified by Brandt et al. (1992). However, their studies suggest grains that are persistent flashers should be 5–10 times less likely to occur than normal K_{2v} grains, which in turn suggests a recurrence rate of ~10%–17%. The higher value of 50% obtained in these data could be due to the internetwork mask preferentially containing persistent flashers rather than normal internetwork grains.

4.4. *Long-Lifetime Oscillations*

During each cycle, a wave may transfer a portion of its energy to the surroundings. Hence, any LLOs, which undergo several complete cycles, are good candidates for chromospheric heating. In all the UV passbands, in both the network and internetwork, all the LLOs occur near the acoustic band. At longer periods, oscillations tend to last for fewer cycles and are even more transient at shorter periods. These LLOs never recur in the same place in both blocks of the data. This suggests that the source that drives the LLO no longer has

TABLE 1
Periodicity of Peak Occurrence Rate and Peak Fourier Power

Wavelength Data Set	Network				Internetwork			
	Wavelet		Fourier		Wavelet		Fourier	
	Center	Width	Center	Width	Center	Width	Center	Width
1550 A	2.441	0.080	2.460	0.141	2.391	0.089	2.408	0.143
1216 A	2.457	0.084	2.462	0.127	2.413	0.093	2.421	0.136
1600 A	2.440	0.081	2.452	0.135	2.391	0.084	2.407	0.136
1700 A	2.443	0.077	2.453	0.136	2.393	0.082	2.408	0.131
1550 B	2.455	0.089	2.479	0.166	2.401	0.088	2.435	0.166
1216 B	2.464	0.090	2.473	0.136	2.414	0.092	2.421	0.137
1600 B	2.453	0.098	2.470	0.140	2.406	0.096	2.422	0.143
1700 B	2.457	0.100	2.563	0.141	2.409	0.093	2.419	0.137
Average	2.451 ± 0.087		2.464 ± 0.140		2.402 ± 0.090		2.418 ± 0.141	

Note.—Centers and 1 σ widths (both in $\log_{10}$ s) of the Gaussian fits to the occurrence rate and Fourier power curves for the first half (block A) and second half (block B) in each bandpass.

sufficient energy to create further oscillations (or if it does create further oscillations, they will be too weak or have short lifetimes and hence will not be detected). Of course, it may be that LLOs do recur, but more than 111 minutes (167×45 s) apart. It is also noted that the lower HOF passbands (1700 and 1600 Å) contain more LLOs than the upper passbands, and whereas 1.5%–2.0% of network pixels contain LLOs, only 0.05% of internetwork pixels display LLOs. Further studies of more LLOs are necessary to confirm these effects.

4.5. *Network-Internetwork Comparison*

From a comparison of the network and internetwork results in all passbands, a few common themes are apparent. As often confirmed before, the network tends to oscillate with a period near 5 minutes. The internetwork, while exhibiting many more oscillations around 3 minutes, contains a peak close to 4 minutes. Table 1 contains a list of the COG fits and 1 σ widths for the Fourier and wavelet approaches. The calculated averages of the COG fits for the Fourier and wavelet approaches agree within the 1 σ widths, and both regions contain a wide range of periodicities. The widths are typically larger in the Fourier than in the wavelet approach, but in both cases a range of $\sim \log_{10}(P) = 2.1$–2.6 is fitted (2.5–7.9 mHz; other work [e.g., Lites et al. 1999; McIntosh et al. 2003] sums over 3–8 mHz). This periodicity range is important to remember when using the 3 and 5 minute oscillations in modeling.

The power of the dominant oscillations in each region was studied using several different methods. Table 2 contains a summary of the occurrence rate of the peak periodicity in both the lifetime-period diagrams (e.g., Figs. 3 and 5) and the COG fits to the average occurrence rate and Fourier power diagrams (e.g., Figs. 4 and 6) in all passbands. It is immediately apparent that the results from the second half of the 1550 Å data set (1550 B) display very low values in both the network and internetwork. These low values may be due to the larger number of saturated pixels, dropped data, and streaks in this part of the data set. Hence, for the following interpretation, the 1550 B data set is ignored.

For the network, the lifetime-period approach (col. [2]) shows an increasing occurrence rate with increasing HOF, from 1700 through 1600 to 1216 Å. It then decreases at 1550 Å. This trend is also prevalent in the values of the COG fit for the occurrence rate (col. [4]) and the COG fit for the Fourier power of data block B (bottom of col. [6]), suggesting

TABLE 2
Values of Peak Occurrence Rate and Peak Fourier Power

Wavelength Data Set (1)	Most Common Oscillation		Peak of Gaussian Fit			
	Occurrence Rate		Occurrence Rate		Fourier Power	
	NWK (2)	INWK (3)	NWK (4)	INWK (5)	NWK (6)	INWK (7)
1550 A	0.212	0.229	0.081	0.073	4.80	4.89
1216 A	0.217	0.257	0.086	0.098	4.61	5.12
1600 A	0.206	0.246	0.079	0.085	4.82	5.15
1700 A	0.188	0.260	0.070	0.090	4.47	5.30
1550 B	0.120	0.138	0.043	0.041	4.33	4.24
1216 B	0.197	0.254	0.079	0.099	4.55	5.13
1600 B	0.179	0.241	0.071	0.088	4.48	4.86
1700 B	0.161	0.259	0.058	0.092	3.96	5.02

Notes.—Frequency of occurrence of the most common oscillation (lifetime-period plots) and frequency of occurrence and Fourier power of the peak of the Gaussian fit of oscillations in the network (NWK) and the internetwork (INWK) for the first half (block A) and second half (block B) in each bandpass. Columns are numbered (2–7) for ease of reference to the text in § 4.5.

oscillations occurring more frequently, leading to an increase in oscillatory power, as waves move up through the atmosphere to the HOF of the 1216 Å passband. As the number, as well as the total oscillatory power, increases, this suggests that waves are exciting oscillations in neighboring regions as they propagate through the atmosphere. Before the waves reach the 1550 Å passband HOF, several of these oscillations are no longer observed. There are a number of possible explanations for this decrease in both occurrence and power of oscillations: (1) waves may either shock or damp between the HOF of 1216 and 1550 Å; (2) at the height at which the canopy closes over completely, the magnetic field lines may be almost horizontal and hence may channel oscillations away from areas defined as network; and (3) upwardly propagating acoustic waves near network areas may undergo mode conversion when interacting with the closing magnetic canopy in the upper chromosphere (Judge et al. 2001), and hence oscillations will change in frequency. It is difficult to determine which one, or combination of two or more, of these explanations is correct.

From a comparison of the Fourier and wavelet approaches in Table 2, it is clear that the internetwork normally has a higher value of oscillatory power (Fourier) and occurrence rate (wavelet) than the network. For the lifetime-period approach (col. [3]), the occurrence rate decreases from the 1700 to the 1600 Å HOF, then increases at the 1216 Å HOF, and decreases again at the 1550 Å HOF. This trend is repeated in the COG fitting approach (col. [5], col. [7] bottom). Therefore, some waves at the 1700 Å HOF must disappear before the 1600 Å HOF. This agrees with the low-lying shocks in internetwork grain simulations of Carlsson & Stein (1992, 1997). Above the 1600 Å HOF, both long- and short-period waves will produce shocks separated by the acoustic cutoff period (Carlsson & Stein 1992), which may explain the increase at 1216 Å. The subsequent decrease at the 1550 Å HOF may then be due to a decreased number of these oscillations propagating to this height.

4.6. *Network-Internetwork Dominance*

Krijger et al. (2001) show that the network oscillatory power exceeds that in the internetwork for all frequencies below $\sim$5 mHz (their Fig. 12). The time-localized nature of wavelet analysis can be used to extend this type of study into the temporal domain. In each bandpass, an average network and internetwork lifetime-period diagram was created (i.e., an average of block A and block B, except at 1550 Å, where only block A data were used; see § 4.5). A comparison diagram was then created by comparing the network occurrence rates to the internetwork occurrence rates at each period and lifetime. Figure 7 shows the resulting network/internetwork comparison for all data sets. In each column, the top part has the same axes and lines as Figure 3 (also Fig. 5). Black parts of the top row of Figure 7 refer to where the network has a greater occurrence rate, whereas gray parts refer to where the internetwork dominates. The middle and bottom rows of Figure 7 are directly comparable to Figures 4 and 6. In these plots, the solid line refers to network data, and a dashed line refers to internetwork data. It is clear from the middle and bottom rows that the network has greater oscillatory power at all periods longer than $\log_{10}(P) = 2.45$ ($P \sim 280$ s; 3.6 mHz). There is also a tendency for this crossover period to decrease with increasing HOF (from $\sim$300 s at 1700 Å to $\sim$250 s at 1550 Å). However, the top row in Figure 7 displays a further feature. If the network dominates for all lifetimes at periods above $\log_{10}(P) = 2.45$, then the resulting plots in the top row should be entirely black to the right of this crossover and entirely gray to the left of this crossover. Instead, there are regions of internetwork domination above $\log_{10}(P) = 2.45$ for a small number of cycles. This mixing is more prevalent for the 1700 and 1600 Å data than for the 1216 and 1550 Å data, suggesting that these short-lifetime, long-period internetwork oscillations are most likely a low-chromosphere phenomenon. There is also some mixing at short periods, which may be examined further by using a higher cadence data set.

5. CONCLUSIONS

A new automated wavelet analysis approach (based on an original idea in Ireland et al. 1999) to *TRACE* quiet-Sun UV data is presented. This permits the extension of the previous Fourier analysis into the time-localized domain. The resulting occurrence rate at specific periods and lifetimes is directly comparable to the results of the classical Fourier approach. The network is found to have a peak occurrence rate periodicity of $\log_{10}(P) = 2.451 \pm 0.087$ ($P = 231 - 346$ s) for a lifetime of 2–3 cycles, with a significant tail of higher period oscillations, while the internetwork is found to have a well-defined peak occurrence rate periodicity of $\log_{10}(P) = 2.402 \pm 0.090$ ($P = 205-309$ s) for a lifetime of 2–3 cycles. Both the network and internetwork show a number of long-lifetime oscillations; however, these do not seem to recur in the same location. Consequently, the driver may have exhausted its energy in generating the LLO. On the other hand, oscillations at 230–280 s, and/or 2–3 cycles, show a tendency to recur at the same spatial position. These are considered good candidates for chromospheric heating. Network oscillations show an increase in occurrence rate and oscillatory power with increasing HOF from 1700 to 1216 Å, possibly as a result of the opening up of the canopy at higher altitudes. In the 1550 Å passband there is a marked decrease in both occurrence rate and oscillatory power, suggesting that any possible waves may have either dissipated, shocked, moved away from the network, or changed in frequency. The network also contains more oscillations around 534 s in the lower HOF than upper HOF passbands, which agrees with the MHD model of Hasan & Kalkofen (1999). In the internetwork there is a decrease in occurrence rate from 1700 to 1600 Å. Hence, some oscillations seem unable to propagate past the low chromosphere. However, the increase at 1216 Å and subsequent decrease at 1550 Å suggests that some waves that do propagate through the low chromosphere may once again excite further oscillations before disappearing higher in the atmosphere. A comparison of the occurrence rate of oscillations in the network and internetwork shows that although the network generally dominates at periods greater than 300 s, for a small number of cycles and long periods the internetwork may dominate. Similarly, regions of network dominance may be found at very short periods (and low lifetimes), where Fourier analysis shows internetwork oscillations to dominate.

A study of the spatial position of pixels displaying different periodicities and lifetimes may answer some of the questions posed in this paper. It may be useful to apply this method to higher cadence *TRACE* quiet-Sun data sets and data from other instruments. It can also be extended into a third spatial region between the network and internetwork (classified as "intermediate" in Krijger et al. 2001). In a wider context, this technique can be used in other areas of solar physics (e.g., active regions) or astronomy in general, where a search for transient,

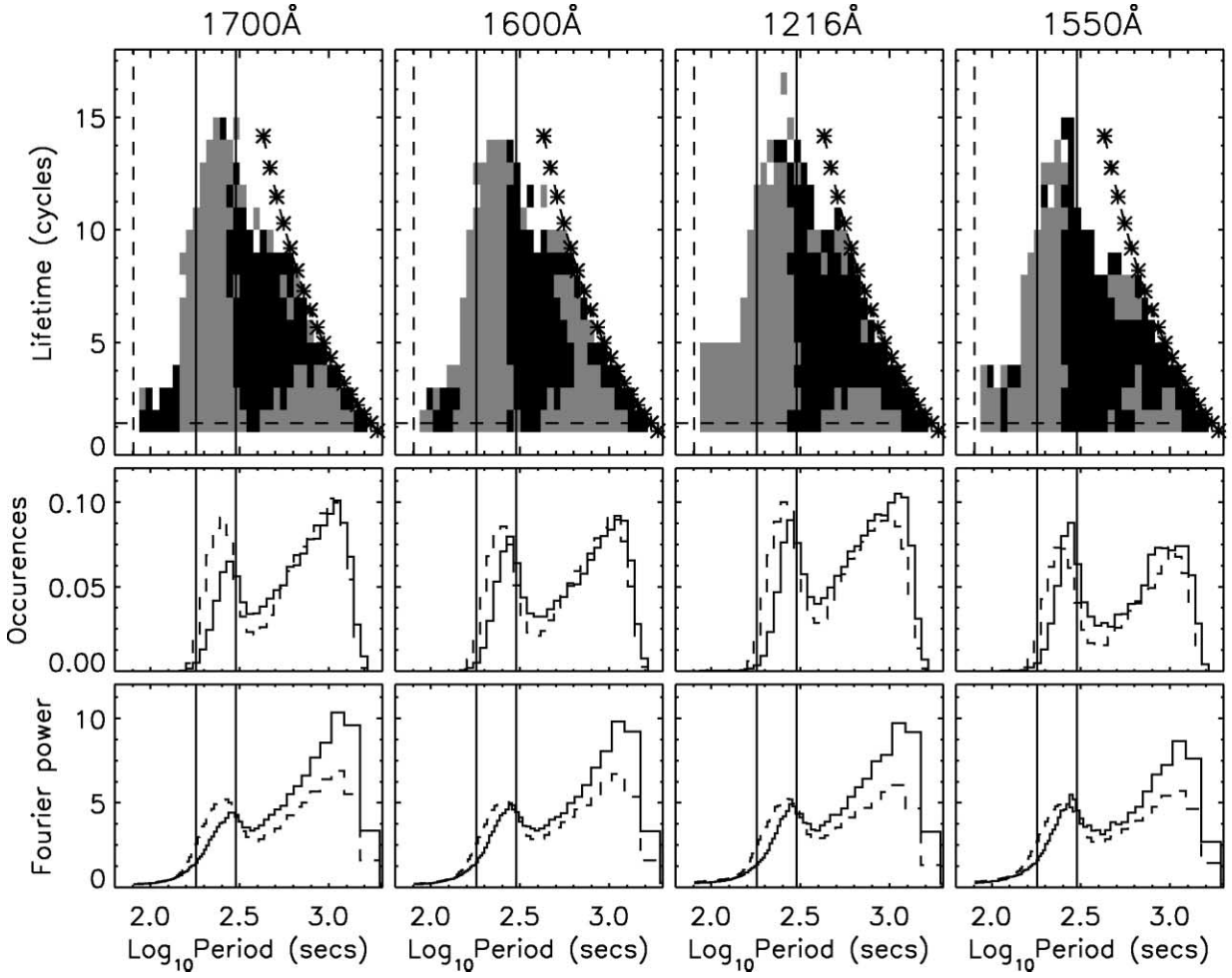

FIG. 7.—Comparison of network and internetwork oscillatory behavior. *Top*: Same axis and lines as Figs. 3 and 5. Gray areas are where the internetwork displays more oscillations; black areas are where the network displays more oscillations, for each period and lifetime. *Middle*: Average occurrence rate per pixel at each period for the network (*solid line*) and internetwork (*dashed line*). *Bottom*: Average Fourier power per pixel at each period for network (*solid line*) and internetwork (*dashed line*). *Columns*: Increasing height of formation from left to right: 1700, 1600, 1216, and 1550 Å

spatially localized, oscillatory power is required (e.g., multi-target wide-field imaging).

This work was funded by a CAST award and Ph.D. studentships from Queen's University Belfast and the Department for Education and Learning (Northern Ireland). F. P. K. is grateful to the Atomic Weapons Establishment (AWE) Aldermaston for the award of a William Penney Fellowship. J. M. A. is thankful to J. Ireland and J. M. Krijger for helpful discussions regarding the wavelet routines and image segmentation. Wavelet software was provided by C. Torrence and G. Compo.[4]

[4] Additional information is available at http://paos.colorado.edu/research/wavelets.

REFERENCES

Banerjee, D., O'Shea, E., Doyle, J. G., & Goossens, M. 2001, A&A, 371, 1137
Baudin, F., Bocchialini, K., & Koutchmy, S. 1996, A&A, 314, L9
Berger, T. E., Löfdahl, M. G., Shine, R. S., & Title, A. M. 1998, ApJ, 495, 973
Bloomfield, D. S., McAteer, R. T. J., Mathioudakis, M., Williams, D. R., & Keenan, F. P. 2003, ApJ, in press
Bocchialini, K., & Baudin, F. 1995, A&A, 299, 893
Bogdan, T. J., et al. 2003, ApJ, 599, 626
Brandt, P. N., Rutten, R. J., Shine, R. A., & Trujillo Bueno, T. 1992, in ASP Conf. Ser. 26, Cool Stars, Stellar Systems, and the Sun, ed. M. S. Giampapa & J. A. Bookbinder (San Francisco: ASP), 121
Carlsson, M., & Stein, R. F. 1992, ApJ, 397, L59
———. 1997, ApJ, 481, 500
Cauzzi, G., Falchi, A., & Falciani, R. 2000, A&A, 357, 1093
Deubner, F.-L., Waldschik, Th., & Steffens, S. 1996, A&A, 307, 936
Farge, M. 1992, Annu. Rev. Fluid Mech., 24, 395
Freeland, S. L., & Handy, B. N. 1998, Sol. Phys., 182, 497
Gallagher, P. T., Phillips, K. J. H., Harra-Murnion, L. K., Baudin, F., & Keenan, F. P. 1999, A&A, 348, 251
Goodman, L. M. 2000, ApJ, 533, 501
Handy, B. N., Bruner, M. E., Tarbell, T. D., Title, A. M., Wolfson, C. J., Laforge, M. J., & Oliver, J. J. 1998b, Sol. Phys., 183, 29
Handy, B. N., Tarbell, T. D., Wolfson, C. J., Korendyke, C. M., & Vourlidas, A. 1999, Sol. Phys., 190, 351
Handy, B. N., et al. 1998a, Sol. Phys., 187, 229
Hansteen, V. H., Betta, R., & Carlsson, M. 2000, A&A, 360, 742
Harrison, R. A., et al. 1995, Sol. Phys., 162, 233
Hasan, S. S., & Kalkofen, W. 1999, ApJ, 519, 899
Hasan, S. S., Kalkofen, W., van Ballegooijen, A. A., & Ulmschneider, P. 2003, ApJ, 585, 1138
Ireland, J., Walsh, R. W., Harrison, R. A., & Priest, E. R. 1999, A&A, 347, 355
Judge, P. G., Tarbell, T. D., & Wilhelm, K. 2001, ApJ, 554, 424
Kalkofen, W. 1997, ApJ, 486, L145

Kneer, F., & von Uexküll, M. 1985, A&A, 144, 443
———. 1986, A&A, 155, 178
———. 1993, A&A, 274, 584
Krijger, J. M., Heinzel, P., Curdt, W., & Schmidt, W. 2003, A&A, submitted
Krijger, J. M., Rutten, R. J., Lites, B. W., Straus, Th., Shine, R. A., & Tarbell, T. D. 2001, A&A, 379, 1052
Leighton, R. B., Noyes, R. W., & Simon, G. W. 1962, ApJ, 135, 474
Lites, B. W., Rutten, R. J., & Berger, T. E. 1999, ApJ, 517, 1013
Lites, B. W., Rutten, R. J., & Kalkofen, W. 1993, ApJ, 414, 345
McAteer, R. T. J., Gallagher, P. T., Williams, D. R., Mathioudakis, M., Bloomfield, D. S., Phillips, K. J. H., & Keenan, F. P. 2003, ApJ, 587, 806
McAteer, R. T. J., Gallagher, P. T., Williams, D. R., Mathioudakis, M., Phillips, K. J. H., & Keenan, F. P. 2002, ApJ, 567, L165
McIntosh, W. S., Fleck, B., & Judge, P. G. 2003, A&A, 405, 769
McIntosh, W. S., & Judge, P. G. 2001, ApJ, 561, 420
Narain, U., & Agarwal, P. 1994, Bull. Astron. Soc. India, 22, 111
Rutten, R. J. 1999 in ASP Conf. Ser. 184, Proc. 3rd Advances in Solar Physics Euroconference: Magnetic Fields and Oscillations, ed. B. Schmieder, A. Hoffman, & J. Staude (San Francisco: ASP), 181
Rutten, R. J., & Uitenbroek, H. 1991, Sol. Phys., 134, 15
Schrijver, C. J., et al. 1998, Nature, 394, 152
Sivaraman, K. R., Gupta, S. S., Livingston, W. C., Damé, L., Kalkofen, W., Keller, C. U., Smartt, R., & Hasan, S. S. 2000, A&A, 363, 279
Torrence, C., & Compo, G. P. 1998, Bull. Am. Meteor. Soc., 79, 61
Wikstøl, Ø., Hansteen, V. H., Carlsson, M., & Judge, P. G. 2000, ApJ, 531, 1150
Worden, J., Harvey, J., & Shine, R. 1999, ApJ, 523, 450